ACS Catalysis

Research Article

Cite This: ACS Catal. 2018, 8, 10306−10315

pubs.acs.org/acscatalysis

Understanding the Impact of Surface Reconstruction of Perovskite Catalysts on CH_4 Activation and Combustion

Felipe Polo-Garzon,[†,‡] Victor Fung,[§] Xiaoming Liu,[‡] Zachary D. Hood,[∥] Elizabeth E. Bickel,[⊥,▽] Lei Bai,[‡,#] Hanjing Tian,[#] Guo Shiou Foo,[†,‡,◆] Miaofang Chi,[‡] De-en Jiang,[§] and Zili Wu*[,†,‡]

[†]Chemical Sciences Division and [‡]Center for Nanophase Materials Sciences, Oak Ridge National Laboratory. Oak Ridge, Tennessee 37831, United States

[§]Department of Chemistry, University of California. Riverside, California 92521, United States

[∥]Electrochemical Materials Laboratory, Department of Materials Science and Engineering, Massachusetts Institute of Technology. Cambridge, Massachusetts 02139, United States

[⊥]Department of Chemical Engineering, Tennessee Technological University. Cookeville, Tennessee 38505, United States

[#]Department of Chemical and Biomedical Engineering, West Virginia University, Morgantown, West Virginia 26506, United States

Supporting Information

ABSTRACT: Methane conversion has received renewed interest due to the rapid growth in production of shale gas. Methane combustion for power generation and transportation is one of the alternatives for methane utilization. However, complete conversion of methane is critical to minimize negative environmental effects from unburned methane, whose noxious effect is 25 times greater than that of CO_2. Although perovskite catalysts have high thermal stability, their low activities for methane combustion prevent them from being utilized on a commercial basis. In this work, we show the impact from reconstruction of surface and subsurface monolayers of perovskite catalysts on methane combustion, using $SrTiO_3$ (STO) as a model perovskite. Several STO samples obtained through different synthetic methods and subjected to different post-synthetic treatments were tested for methane combustion. Through top surface characterization, kinetic experiments (including isotope labeling experiments) and density functional theory calculations, it is shown that both surface segregation of Sr and creation of step surfaces of STO can impact the rate of methane combustion over an order of magnitude. This work highlights the role of surface reconstruction in tuning perovskite catalysts for methane activation.

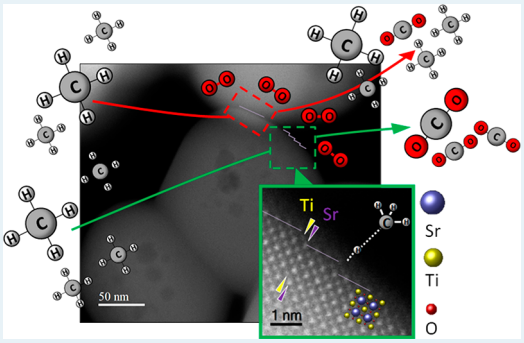

KEYWORDS: *surface reconstruction, perovskite catalysts, methane activation, methane combustion, step-sites*

Downloaded via GEORGIA INST OF TECHNOLOGY on September 14, 2022 at 19:16:00 (UTC).
See https://pubs.acs.org/sharingguidelines for options on how to legitimately share published articles.

INTRODUCTION

The production of natural gas, composed mostly of methane, has increased significantly in recent years and its growth is projected to be steady over the coming decades.[1] Methane is widely used in power generation, transportation, and heating applications.[2−4] Flame combustion of methane, however, produces harmful NO_x compounds at the high temperatures involved in this process.[2,4] Therefore, catalytic combustion of methane at lower temperatures is an environmentally advantageous process. Nonetheless, the reduction of reaction temperatures when employing a suitable catalyst may lead to unburned methane, which has a noxious effect 25 times greater than that of CO_2.[2,5] Thus, research efforts seek catalysts with outstanding performance (full methane conversion at low temperatures) and long-term thermal stability.

Although expensive noble metal catalysts have shown the highest rates for methane combustion, their poor thermal stability has turned researchers' attention toward inexpensive and thermally stable alternatives, such as perovskites.[2−4,6−8] Perovskites are mixed metal oxides of general formula ABO_3, where A represents a lanthanide, alkali or alkaline component and B represents a transition metal. Perovskites have shown excellent thermal stability (up to 1000 °C), resistance to sintering of substituted metals, and high oxygen mobility, which is beneficial for typical reduction−oxidation (redox) processes such as CH_4 combustion.[8,9] The effects of surface reconstruction of perovskites on catalysis have been explored only in the past decade,[10−17] revealing the underexplored catalytic potential of these materials. In this paper, we address in detail the effect that surface reconstruction of perovskites has on CH_4 activation. The model perovskite catalyst under study is $SrTiO_3$ (STO), and we explore its catalytic activity for CH_4 combustion, aiming to unveil critical findings toward the activation of CH_4. Since surface reconstruction is common for

Received: June 13, 2018
Revised: September 19, 2018
Published: September 24, 2018

© 2018 American Chemical Society

DOI: 10.1021/acscatal.8b02307
ACS Catal. 2018, 8, 10306−10315

perovskites, as shown in our previous work[16,17] as well as by others,[10−15,18−21] we believe the present work has the potential to impact the field of methane conversion over perovskite catalysts in general.

Although STO is not among the most active perovskite catalysts for methane combustion due to its limited redox properties, its excellent thermal stability and the recent knowledge obtained on its reconstruction properties[10,16,17,21−29] make this catalyst a well-suited model system for fundamental studies of surface tunability toward enhanced CH_4 activation. Redox properties including oxygen vacancies and lattice oxygen mobility of perovskite catalysts, critical for methane combustion, are often tuned by varying the composition of B site or doping both A and B sites. For example, lanthanum manganite and cobaltite have shown superior activity for methane combustion among the perovskite family.[7] These strategies often lead to the change of crystal structure and surface composition, making it difficult to establish the structure−catalysis relationship. The present study on the effect of surface reconstruction on the rate of methane combustion was conducted on a set of STO samples with the same crystal structure and elemental composition, allowing the study of other factors relevant for catalysis while holding the redox contributions constant. It is shown that tuning the relative composition of Sr at the STO surface can increase the reaction rate of methane combustion over an order of magnitude. Although STO remains a low-activity catalyst, the fundamental insights gained herein open a new possibility for improving the reactivity of other perovskites via controlling the surface reconstruction, which can be a general approach for perovskites.

In this work, we use a combination of experimental and computational approaches to relate the subsurface layer composition with top-surface composition, as well as top surface reconstruction with the performance of undoped STO catalysts. Step sites of the Sr-terminated surface are identified as the active sites for CH_4 homolytic activation. Interestingly, others have arrived at a similar conclusion, reporting that CH_4 activates over steps and corners of MgO on a Li-doped MgO catalyst.[30] This work shows evidence for the role of step sites on CH_4 activation over perovskite catalysts and relates the reconstruction of the catalyst surface (and subsurface) to rates of CH_4 combustion over a broad set of samples synthesized in various ways.

EXPERIMENTAL DETAILS

Materials. Strontium titanate (STO) and strontium oxide (SrO) were commercially obtained from Sigma−Aldrich. Titanium oxide in the rutile phase was purchase from Alfa Aesar. Argon, helium, 10% CH_4/Ar (or 10% CH_4/He), 5% $^{16}O_2$/He, 2% CO_2/Ar, and 10% CD_4/He were purchased form Airgas. 2% CO/Ar/He was purchased from Air Liquide. 2% $^{18}O_2$/He was purchased from Sigma−Aldrich.

Chemical Etching. Sr from top surface layers was etched off STO samples by use of a 0.2 M aqueous solution of HNO_3 (20 mL of solution/g of catalyst) as previously performed by Peng et al.[14] and also implemented in our previous publications.[16,17] Briefly, the catalyst sample was submerged in the acid solution, and the mixture was vigorously stirred for a few seconds and left still for 1 day at room temperature. The catalyst was then washed with deionized water and centrifuged at least four times at 12 000 rpm for 10 min. The separated solid was dried at 60 °C overnight in a vacuum oven.

Incipient Wetness Impregnation. Sr was deposited on the sample surface by means of incipient wetness impregnation (IWI), following a procedure reported previously.[31,32] Briefly, $Sr(NO_3)_2$ was dissolved in water and the resulting solution was impregnated onto the catalyst. Impregnation was performed in a glass dish such that the solid was homogeneously wetted with the solution. The mixture was placed in the drying oven at 110 °C for approximately 16 h at 110 °C. Before samples were used for catalytic tests, they were calcined at 750 °C for at least 5 h.

Hydrothermal Synthesis. A set of STO catalysts was synthesized by the hydrothermal (HT) method.[33−35] The three samples synthesized via this method had cubic, truncated cubic, and dodecahedral shapes after calcination at 550 °C for 4 h in air. For this work, however, the samples are further calcined at 750 °C for 5 h in air to achieve the thermodynamically stable shape of the sample under reaction conditions. After calcination at 750 °C, the samples appear as cubic with irregular truncations. The synthetic procedure has been thoroughly described previously.[17] Briefly, 20 g of ethanol, 12 g of 1,2-propanediol, or 1.2 g of pentaerythritol were added to 25 mL of deionized water, for the synthesis of cubes, truncated cubes, or dodecahedral STO nanocrystals, respectively. Subsequently, 0.26 mL of titanium(IV) chloride was added dropwise into the solution, followed by 30 mL of LiOH aqueous solution containing 3.78 g of $LiOH·H_2O$ and by 10 mL of $SrCl_2$ aqueous solution containing 0.63 g of $SrCl_2·6H_2O$. The mixture was stirred after each addition. The resultant mixture was placed in a Teflon-lined stainless-steel autoclave (Parr 5000 multireactor stirrer system). The autoclave was heated at 180 °C for 48 h. After cooling to room temperature, the sample was washed and centrifuged several times. The sample was then dried at 100 °C for 12 h. Finally, the sample was calcined in air at 550 °C for 4 h and then at 750 °C for 5 h.

Brunauer−Emmett−Teller Surface Area. A Micromeritics Gemini 2375 surface area and pore size analyzer was used to perform nitrogen physisorption at −196 °C. Before any measurements, the samples were calcined at 750 °C in air for 5 h to measure surface areas under reaction conditions. The catalysts were degassed for 1 h prior to measurement. Surface areas were calculated by the BET method.[36]

X-ray Diffraction. X-ray diffraction (XRD) was used to identify the crystal structure of the samples studied. The PANalytical Empyrean system was employed for the measurements, using Cu Kα radiation. Incident angles (2θ) were between 5° and 90°.

Low-Energy Ion Scattering Analysis. Low-energy ion scattering (LEIS) measurements were performed at Lehigh University in an ION-TOF Qtac100 spectrometer (ION-TOF GmbH, Münster, Germany). The sample was outgassed within the spectrometer preparation chamber in vacuum at 100 °C for a few minutes. In some cases, O_2 was then introduced into the preparation chamber, and the temperature was ramped to 500−600 °C and held for 30−60 min for in situ thermal pretreatment. After cooling and chamber evacuation, the sample was then analyzed by LEIS. Charge neutralization was invoked during spectra acquisition and sputtering. Spectra were collected by use of 3 keV of He^+ at 3×10^{14} ions·cm^{-2} or 5 keV of Ne^+ at 1×10^{14} ions·cm^{-2} per profile cycle. Sputtering of the samples, to obtain the depth profile, was done with 0.5 keV of Ar^+ at 5×10^{14} ions·cm^{-2} per profile cycle.

Sr composition [Sr/(Sr + Ti)] reported in this work is calculated by assuming that the Sr composition is 50% at 5 nm depth for a commercial STO sample without any pretreatment.

DOI: 10.1021/acscatal.8b02307
ACS Catal. 2018, 8, 10306−10315

Inductively Coupled Plasma Measurements. Inductively coupled plasma (ICP) measurements were performed by Galbraith Laboratories Inc. Two representative samples were sent for ICP analysis: a STO sample synthesized via the HT method (catalyst 12 in Table S1) for which traces of Li were tested, and a control sample (Sr/TiO_2, catalyst 16 in Table S1), to obtain the exact amount of Sr deposited on the surface.

X-ray Photoelectron Spectroscopy. STO samples were calcined ex situ in O_2 at 750 °C for 5 h before X-ray photoelectron spectroscopic (XPS) measurements. XPS spectra were collected for each powder sample on a Thermo K-Alpha XPS system with a spot size of 400 μm and a resolution of 0.1 eV. All spectra were processed by use of Thermo Avantage, which is a software package provided through Thermo Scientific.

Kinetic Measurements. CH_4 combustion was performed in a fixed-bed reactor by use of an AMI-200 Altamira instrument. Before kinetic measurements were performed, each sample was pretreated in situ under 50 mL/min 5% O_2/He at 750 °C for 5 h. For all results presented in the main text, 30 mg of catalyst (except for 11 mg for sample 14 in Table S1) were diluted in quartz beads (diluent/catalyst = 13 by mass), both sieved to particle size 177−250 μm, were loaded into a U-tube reactor to perform the kinetic measurements. CO and CO_2 were the predominant products observed. Products were analyzed by use of a Buck Scientific Model 910 gas chromatograph (GC) equipped with a flame ionization detector and a HayeSep-D column. The GC response factor was calibrated for all compounds.

Temperature-programmed reaction (TPR) experiments were performed at a slow heating rate (1.5 °C/min) that allowed reproduction of conversions and selectivities at steady state (Figure S1) and browsing of a wide range of temperatures for the various samples tested in this study (Figure S2). For fair comparison of rates among a set of catalysts operating under differential conditions at different temperature ranges, rates were extrapolated after fitting the data at conversions no greater than 17% to a simple rate expression:[8] rate = $k(P_{CH_4})^n(P_{O_2})^m$. Tests regarding mass transfer limitations and the effect of space velocity are reported in Figures S4−S6.

Fourier Transform Infrared Spectroscopy. Fourier transform infrared (FTIR) spectroscopic measurements were performed in a Thermo Nicolet Nexus 670 FTIR spectrometer with a mercury cadmium telluride (MCT) detector. The catalyst samples were calcined ex-situ at 750 °C and then loaded into a crucible placed in a diffuse reflectance infrared Fourier transform spectroscopy (DRIFTS) cell (Pike Technologies). The catalysts were activated in situ under 30 mL/min argon at 450 °C for 1 h. After pretreatment, the temperature of the cell was lowered to −146 (±4) °C and a background spectrum was collected. Following the background collection, 7% CH_4/Ar at 30 mL/min flowed through the cell for 10 min; then the gas flow was switched to 30 mL/min argon. Spectra were recorded with 32 scans at a resolution of 4 cm^{-1} during the adsorption/desorption processes.

Electron Microscopy. High-angle annular dark-field scanning transmission electron microscopy (HAADF-STEM) was carried out on an aberration-corrected FEI Titan S 80−300 TEM/STEM operated at 300 kV. Imaging was performed with a probe convergence angle of 30 mrad and a large inner collection angle of 65 mrad. All images were taken after calcination of the samples at 750 °C for 5 h.

Density Functional Theory. Periodic density functional theory (DFT) calculations were performed with the Vienna ab initio Simulation Package (VASP).[37,38] The PBE-GGA functional[39] was used for electron exchange and correlation. The electron−core interaction was described by use of the projector-augmented wave method (PAW).[40,41] An energy cutoff of 450 eV and a 3 × 3 × 1 Monkhorst−Pack scheme[42] were used for the calculations. A 3 × 3 supercell of the slabs was created from the unit cell, and van der Waals correction were implemented. Transition states were found by use of the climbing-image nudged elastic band (CI-NEB) method[43] with a force convergence of 0.05 eV/Å.

RESULTS AND DISCUSSION

Surface and Subsurface Composition. Two sets of STO catalysts were studied. The first set was generated by treating commercially obtained STO (STO_{com}) with a 0.2 M solution of HNO_3 and/or impregnating it with Sr via IWI. The chemical etching (HNO_3 treatment) exposed Ti cations at the surface,[16] whereas impregnating the sample with Sr increased the surface composition of Sr. The second set of STO catalysts (STO_{HT}) was synthesized in-house by the HT synthetic method. The solvent used in the HT method led to different surface reconstruction of the catalysts, as shown later in this paper. The compositions of the top surface layer from LEIS analysis and BET surface areas of all the studied samples are provided in Table S1. All STO samples presented the perovskite crystal structure without detectable additional phases via XRD (see Figure S7).

As lithium was used for the synthesis of STO_{HT} samples, the Li content in one of the STO_{HT} samples (catalyst 12 in Table S1) was analyzed via ICP. It was found that lithium was present at 0.11 wt %. Other impurities were also detected at the top surface of the catalysts via LEIS (Figure S8). Unfortunately, lithium is not directly detectable by LEIS with 3 keV of He^+ as a probe, which was used in the present work. To analyze the concentration of impurities near the surface of the catalysts, XPS measurements were performed on select STO samples (Figure S9 and Table S3). Traces of F, Na, Cl, and C were detected at the near-surface region; however, Li was not. No direct correlation can be drawn between the presence of impurities and the trends in catalytic activity (see discussion in Supporting Information). Rather, the concentration of Sr at the surface and the density of step sites are the most relevant reactivity descriptors, as explained below.

The reconstruction of perovskites at the surface is not only influenced by postsynthetic methods and synthetic conditions described above, but it is also known that thermal treatment of the samples induces enrichment of Sr at the surface.[16] After impregnation of commercial STO (and chemically etched commercial STO) with Sr, it was observed that even mild heat treatment in air (110 °C for 16 h) promoted enrichment of the top surface and subsurface monolayers with Sr, and increased treatment temperature (750 °C) promoted even further segregation of Sr at the surface (Figure 1a,b). Nonetheless, as seen in Figure 1a, the impregnated commercial STO sample (Sr/STO) treated at 110 °C showed only a slight increase in Sr concentration toward the surface when compared with the untreated STO sample, whereas the heat treatment at 750 °C notoriously increased the concentration of Sr at the surface and subsurface.

The composition of the top surface correlates with the composition of sublayers independent of the various synthetic

DOI: 10.1021/acscatal.8b02307
ACS Catal. 2018, 8, 10306−10315

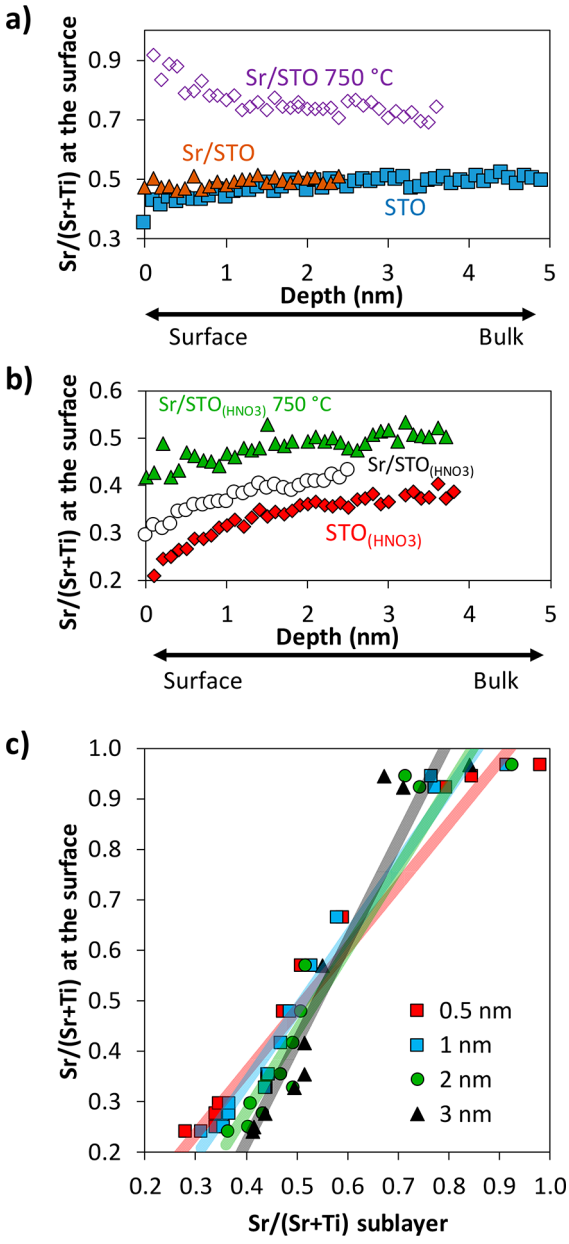

Figure 1. Surface Sr/(Sr + Ti) cation intensity ratio as a function of probing depth using LEIS analysis for (a) commercial STO, commercial STO impregnated with Sr and dried at 110 °C overnight (Sr/STO), and Sr/STO calcined at 750 °C and (b) chemically etched STO ($STO_{(HNO_3)}$), $STO_{(HNO_3)}$ impregnated with Sr and dried at 110 °C overnight ($Sr/STO_{(HNO_3)}$), and $Sr/STO_{(HNO_3)}$ calcined at 750 °C. (c) Correlation between the concentration of Sr at the top surface of the catalyst and the concentration of the subsurface at different probing depths for all STO catalysts studied in this work. Refer to Supporting Information for detailed information about these samples.

and posttreatment methods (impregnation, chemical etching, and heat treatment) employed. These methods were used to obtain STO samples with a wide range of surface compositions (Figure 1c). See representative LEIS spectra and full depth profiling in Figures S8 and S10. This is clear evidence of the role that STO bulk plays in stabilizing certain surface compositions of the catalyst. In addition, catalysts with the perovskite crystal structure showed activity for CH_4 combustion, whereas a Sr-impregnated TiO_2 sample did not show catalytic activity, suggesting that the bulk plays a role in this catalytic process (presented in the next section). As will be shown, the composition of the top surface is a surface reactivity descriptor for a subset of perovskites, and therefore, one can draw a correlation between the composition of catalyst subsurface and catalyst performance.

Catalyst Performance. The various STO catalysts were tested for CH_4 combustion under rich ($O_2/CH_4 = 4$) and lean ($O_2/CH_4 = 1.6$) conditions. Variation of CH_4 consumption rate and CO_2 selectivity with respect to the composition of the top surface at $O_2/CH_4 = 4$ is presented in Figure 2.

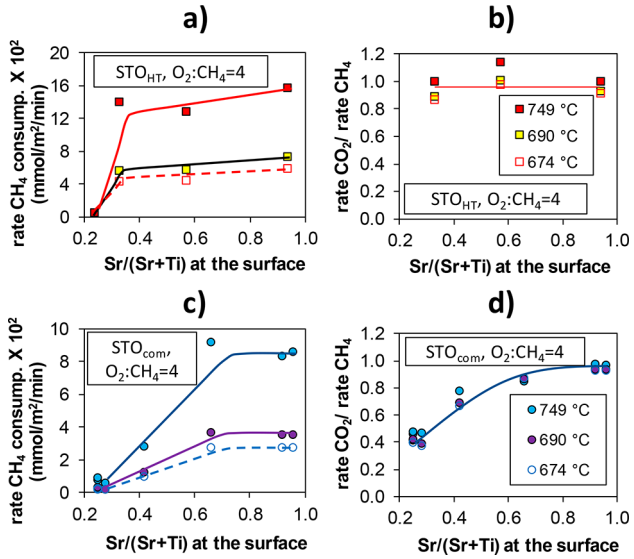

Figure 2. (a, c) Rate of methane conversion versus composition of top catalyst layer at different temperatures for (a) STO catalyst synthesized via the HT method (STO_{HT}) and (c) STO catalyst after chemical etching or IWI of commercial STO (STO_{com}). (b, d) CO_2 selectivity versus composition of top catalyst layer at different temperatures for (b) STO_{HT} and (d) STO_{com}. Reaction conditions: 30 mg of catalyst (11 mg for STO_{HT} with 24% surface Sr), 1.4 atm, feed consists of 51 mL/min 1.1% CH_4, 4.5% O_2, balance Ar + He. Values greater than unity for the ratio of rate of CO_2 consumption to rate of CH_4 consumption arise from extrapolation of reactivity data, as explained under Experimental Details.

The samples showed vastly different rates for CH_4 combustion under both rich and lean O_2 concentrations (Figure 2 and Figure S11, respectively), with rates per surface area differing by more than an order of magnitude for different surface compositions. Selectivity toward complete combustion (CO_2) was weakly dependent upon temperature. As a control, TiO_2 and Sr/TiO_2 (1.6 mg of $Sr{\cdot}m^2$ of TiO_2) were tested for CH_4 combustion and showed no activity, different from the catalytic activity showed by the impregnated STO samples (0.1−1 mg of $Sr{\cdot}m^2$ of STO). This highlights that the relative composition of cations at the surface and subsurface, as well as their arrangement (related to the crystal structure), are critical for methane combustion.

Kinetic Isotopic Effect. As seen in Figure 2, enrichment of the surface with Sr promotes the rates of CH_4 combustion over a wide range. To unveil the underlying catalytic phenomena leading to this trend, kinetic isotopic experiments were performed, initially to identify the part of the mechanism where the rate-determining step (RDS) is located, and posteriorly to compare the energetic barriers associated with overcoming the

DOI: 10.1021/acscatal.8b02307
ACS Catal. 2018, 8, 10306−10315

Table 1. Kinetic Isotopic Effects for Select STO Samples[a]

			CD_4 KIE[b]				$^{18}O_2$ KIE[c]			
			conversion (%)				conversion (%)			
sample	Sr/(Sr + Ti) at surface	T (°C)	CH_4 + $^{16}O_2$	CD_4 + $^{16}O_2$	KIE	100 × (KIE/KIE_{theor})[d]	CH_4 + $^{16}O_2$	CH_4 + $^{18}O_2$	KIE	100 × (KIE/KIE_{theor})[e]
STO_{HT}	0.39[f]	674	15.6	10.4	1.50	84	16.7	14.5	1.15	75
STO_{com}	0.72	674	33.9	25.6	1.32	74	35.3	32.5	1.09	71
STO_{HT}	0.96[f]	674	15.7	11.0	1.42	79	16.9	14.6	1.16	76

[a]Samples were either obtained commercially (STO_{com}) or synthesized in-house by the HT method (STO_{HT}). [b]Reaction conditions: 30 mg of catalyst, 1.4 atm, feed consists of 55 mL/min 1.0% CH_4, 1.7% O_2, balance Ar + He. [c]Reaction conditions: 30 mg of catalyst, 1.4 atm, feed consists of 51 mL/min 1.1% CH_4, 1.8% O_2, balance Ar + He. [d]CD_4 KIE_{theor} = 1.79. [e]$^{18}O_2$ KIE_{theor} = 1.53. [f]Taken from ref 17.

RDS for the samples under study. The kinetic isotopic effect (KIE) was measured as the ratio between the rate of reaction with an unlabeled reactant mixture (CH_4 + $^{16}O_2$), and the rate of reaction with an isotopic reactant mixture. The two isotopic mixtures used were CD_4 + $^{16}O_2$ (CD_4 KIE) and CH_4 + $^{18}O_2$ ($^{18}O_2$ KIE). The KIE was measured under the same reaction conditions (for at least 1 h time-on-stream) for select samples covering most of the range of surface compositions studied herein. In this initial stage, reaction conditions were chosen such that fractional conversions were obtained for both regular and labeled reactants, while the temperature, pressure, space velocity, and catalyst mass were held constant. Due to the different reaction rates and surface areas of the catalyst samples, differential conditions (conversion below ~15−17%) were not achieved while all reaction conditions were held constant. However, in this initial comparison (Table 1), the objective is to compare CD_4 KIE to $^{18}O_2$ KIE for each sample, not to draw comparisons among samples. As shown in Table 1, the RDS was found in the part of the reaction mechanism corresponding to the dehydrogenation of CH_4, not the dissociation of O_2, as CD_4 KIE (1.32−1.50) is larger than $^{18}O_2$ KIE (1.09−1.16) in all cases. The theoretical KIE is greater for the CH_4/CD_4 switch (1.79) than for the $^{18}O_2/^{16}O_2$ switch (see Supporting Information for details), and one can expect intrinsically higher CD_4 KIE than $^{18}O_2$ KIE; however, on a normalized basis (column 100 × KIE/KIE_{theor} in Table 1), the kinetic isotopic effect is still generally greater for CD_4 than for $^{18}O_2$. This shows that O_2 dissociation is not the major kinetically relevant step for CH_4 combustion over perovskites.

To rule out the effect of reaction conversion on the measured KIE, in a second stage, we have conducted TPR experiments over a wide range of temperatures, and the rates were extrapolated after fitting the data at conversions no greater than 17% to a simple rate expression (see Experimental Details and Supporting Information). The values for CD_4 KIE (measured under differential conditions) as a function of the composition of the top catalyst surface are shown in Figure 3. All the measured CD_4 KIE for STO samples in this study were very similar, suggesting similar energetics for the transition state involved in methane activation for the samples studied. The differences in the rate of methane combustion (Figure 2) can then be attributed to different surface density of active sites, and therefore, one can hypothesize that the density of active sites increases as the surface becomes richer in Sr. However, this hypothesis is true when studying the two sets of STO catalysts separately (STO_{com} and STO_{HT}).

Although each set of STO samples (STO_{com} and STO_{HT}) shows a correlation between the rate of methane consumption and the concentration of Sr at the surface, it is clear that STO_{HT} samples exhibit considerably higher rates when

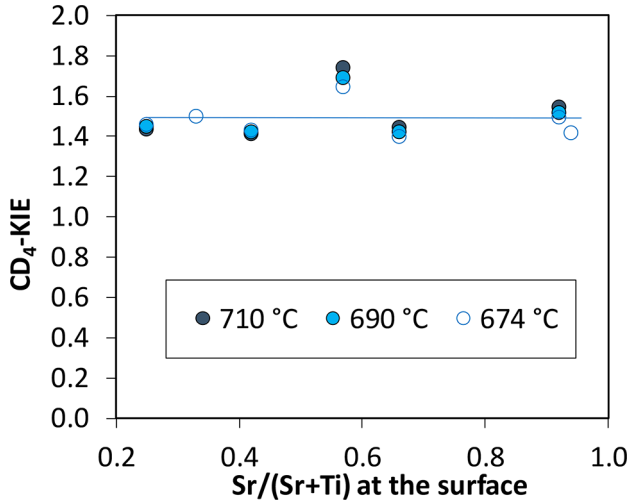

Figure 3. CD_4 KIE at different temperatures, measured under differential conditions, for CH_4 consumption rate over STO catalysts under study. Reaction conditions: 30 mg of catalyst, 1.4 atm, feed consists of 55 mL/min of 1.0% CH_4, 1.7% O_2, balance Ar + He.

compared with STO_{com} samples (Figure 2a,c) at similar surface Sr concentrations. This difference is due to the increased density of the most active sites (step sites) in the STO_{HT} samples when compared to the STO_{com} samples, as explained in the following sections.

Electron Microscopy. Although LEIS is a powerful technique to characterize the composition of the surface with monolayer precision, this technique does not provide information about the arrangement of atoms at the surface. For that purpose, high-angle annular dark-field scanning transmission electron microscopy (HAADF-STEM) was employed to image the surface termination of select STO samples (see Figure 4 and Figures S12 and S13). Three samples were carefully chosen for imaging: the sample with the highest rate of CH_4 consumption (Figure 4a) and two samples with similar surface composition but significantly different reaction rates (Figure 4b,c). In general, for all the particles imaged, the lattice ends with Sr atoms enriched at the (100) and (010) facets, while both Sr and Ti are exposed when the lattice terminates with the (110), (130), (140), (4−10), and (450) facets. The higher index terminations [(130), (140), (4−10), and (450)] are stepped surfaces, which are found to be most abundant on the most active STO_{HT} sample with 94% surface Sr (Figure 4a), followed by a STO_{HT} sample with 57% surface Sr (Figure 4b) and a STO_{com} sample with 66% surface Sr (Figure 4c). Interestingly, the rate of CH_4 consumption is qualitatively related to the observed fraction of stepped terminations, as

DOI: 10.1021/acscatal.8b02307
ACS Catal. 2018, 8, 10306−10315

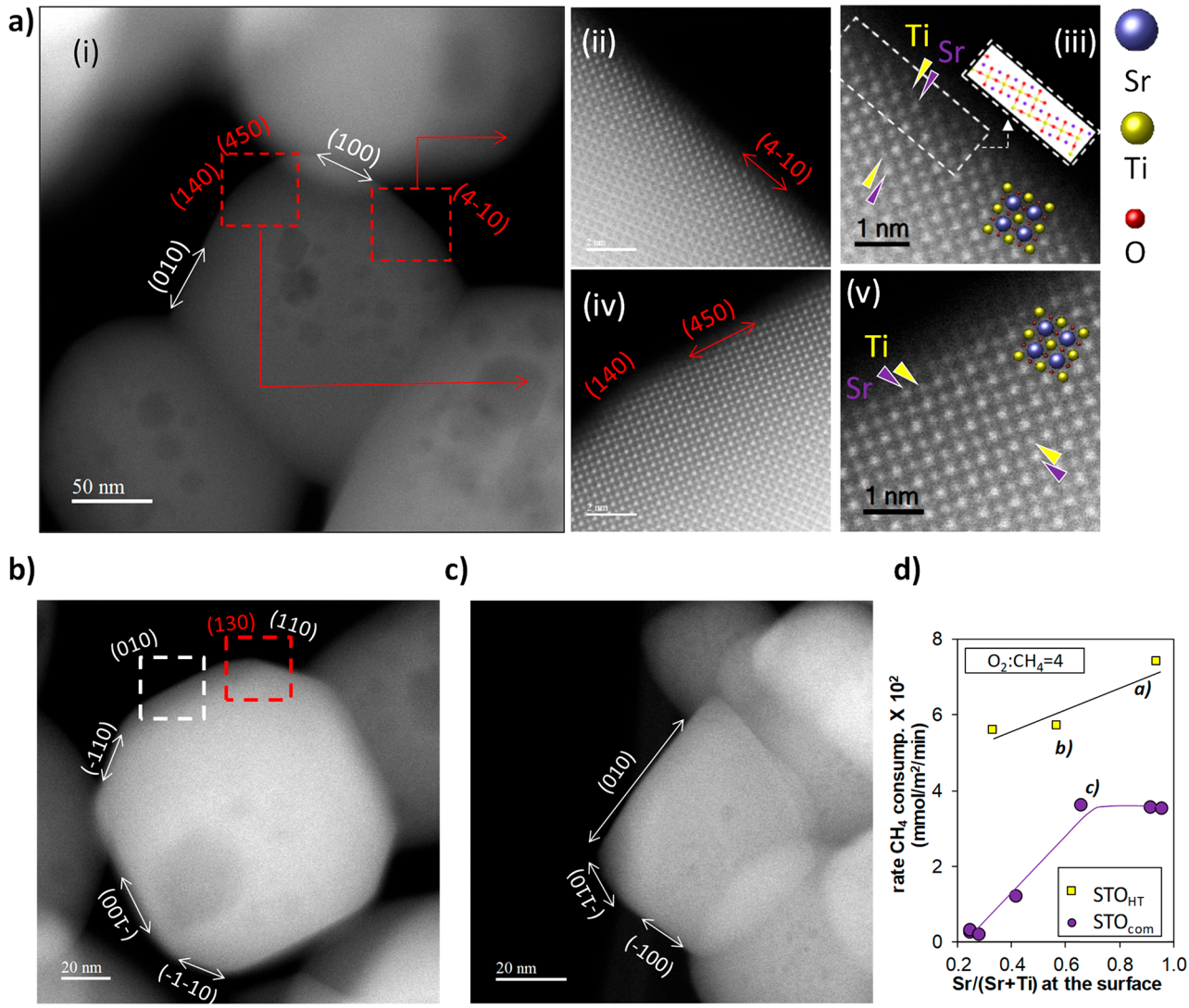

Figure 4. HAADF-STEM images of STO particles (after calcination at 750 °C for 5 h) recorded along [001] zone axis. The labels a, b, and c can be correlated with the results of reactivity displayed on the bottom-right corner (graph d). Samples a and b are STO synthesized via the HT method with 94% and 57% Sr at the surface, respectively. Sample c is a STO sample obtained commercially. Reactivity data have been presented in Figure 2 but are recollected to ease the discussion of the results. Panels ii,iii and iv,v are close examinations of the boxed regions in panel i. Facets are interpreted in the images. The intensity, *I*, in the HAADF-STEM image is in direct proportion to the atomic number, and thus brighter contrast indicates Sr while weaker contrast indicates Ti. However, O contrast is too weak to be observed. Schematic models are shown in panels iii and v. Close examinations of particles b and c are reported in Supporting Information.

displayed in Figure 4d. Furthermore, it is seen from samples b and c in Figure 4d that the concentration of Sr at the surface does not necessarily correlate with the density of step sites, since these two samples present very similar surface composition (57% and 66%, respectively) and yet a different concentration of step sites. It is worth mentioning that only after 750 °C treatment in O_2 (as performed before kinetic measurements in this study) does the surface of the catalyst STO, synthesized via the HT method with 94% surface Sr composition (sample a in Figure 4), develop step terminations. Treatment at 550 °C in O_2 results in a cubic structure terminated predominantly with (100) facets.[17] The exact reason behind the different reconstruction behaviors of commercial and STO_{HT} samples is not within the scope of this study.

Density Functional Theory Calculations. To test if the abundance of surface step sites is responsible for enhanced rates from a reaction-mechanism perspective, periodic DFT calculations were performed to find the homolytic and heterolytic C−H activation energies for methane dissociation on representative surface terminations of STO (see Table 2 and Figure 5). Initially, low-index pristine terminations including (111), (110), and (100) were tested for C−H bond cleavage, and they showed similar activation energies for the most favorable heterolytic cleavage. In homolytic cleavage, a hydrogen atom from CH_4 binds a surface oxygen, creating a free methyl radical. In heterolytic cleavage, a carbanion is created and attached to a surface metal atom. For a pristine (100) facet, the surface can be fully terminated on either Sr or Ti, and it can also have a mixed Sr−Ti termination when step sites are introduced. The pristine facets (110) and (111) can be terminated only with a mixed Sr−Ti layer.

Due to its versatility, the low-index (100) facet was used to model defect (or nonpristine) surfaces, as shown by HAADF-STEM (Figure 4). Since the catalysts studied showed surface Sr compositions between 20% and 96%, the activity of mixed Sr−Ti sites was tested (Ti-doped). As shown in Table 2, for

DOI: 10.1021/acscatal.8b02307
ACS Catal. 2018, 8, 10306−10315

Table 2. DFT-Calculated Adsorption Energies for CH_4 and Activation Energies for Homo- and Heterolytic C−H Bond Cleavage Pathways over STO Surfaces

facet	termination	pathway	E_{ads} (eV)	E_{act} (eV)	ΔH (eV)
(111)	Sr and Ti	hetero	−0.13	1.13	0.19
(110)	Sr and Ti	hetero	−0.21	1.03	0.90
(100)	Sr pristine	homo	−0.10	2.43	1.46
(100)	Ti pristine	hetero	−0.34	0.98	0.71
(100)	Sr (Ti-doped)	hetero	−0.21	0.60	−0.38
(100)	Ti step	hetero	−0.19	0.55	0.21
(100)	Sr step	homo	−0.10	0.32	−3.68
(4−10)	Sr step	homo	−0.14	0.14	−3.72

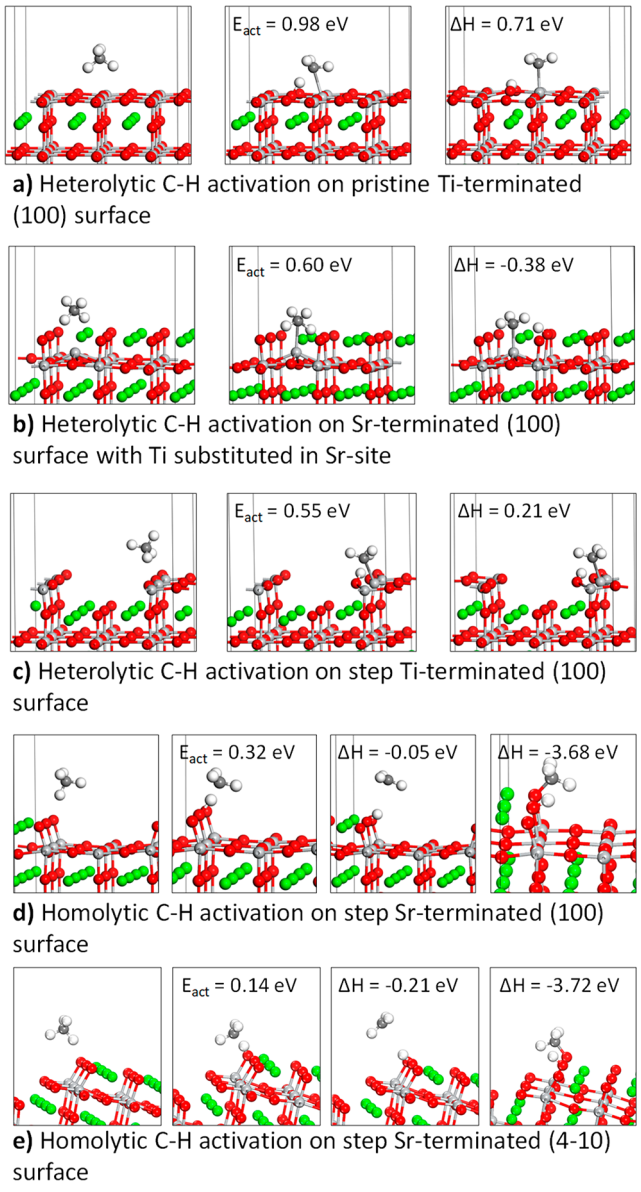

Figure 5. DFT structures of CH_4 dissociation for select terminations of (100) STO surface. Color code: Sr, green; Ti, light gray; O, red; C, dark gray; H, white.

the low-index terminations [(111), (110), and (100)], the STO(100) facet with the Sr step has the lowest activation energy for methane C−H cleavage, 0.32 eV. Substitution of a Ti atom on the Sr-terminated (100) surface (Figure 5b) gave an activation energy for the cleavage of the C−H bond of 0.60 eV, which is lower than the activation energies obtained with any pristine surface (0.98−2.43 eV). As shown in the previous section, one can qualitatively relate the abundance of step sites to increased rates of reaction (Figure 4). Indeed, homolytic dehydrogenation on the Sr-terminated stepped surface (rather than the Ti-terminated stepped surface as shown in Figure 5c) presented the lowest activation barrier (0.32 eV; Figure 5d), and it is therefore suggested that this surface structure provides the most active site for the cleavage of the C−H bond. The Ti-terminated stepped surface showed a less favorable activation energy (0.55 eV). This agrees with reactivity tests and microscopy results, which show that enrichment of Sr at the surface (and subsurface) and creation of step sites enhance rates for CH_4 combustion.

To corroborate our conclusion, homolytic cleavage on the higher-index (4−10) termination, observed via microscopy (Figure 4a,iii), was tested. The initial, transition-state, and final structures of CH_4 activation were very similar on the Sr-stepped (100) and (4−10) terminations (Figure 5d,e, respectively), and the stepped Sr termination remains the one with the lowest activation energy among the terminations tested.

The Rideal−Eley (RD) and Mars−Van Krevelen (MVK) mechanisms have been reported for CH_4 catalytic combustion over perovskites.[7,8] Independent from the mechanism, we have identified the RDS in the dehydrogenation of methane, and the homolytic C−H cleavage has been identified as the most favorable pathway. Creation of the methyl radical can lead to subsequent gas-phase reactions,[44] and thus, this step dictates the rate of reaction.

Infrared Spectroscopy. As observed in Table 2, the adsorption energy of physisorbed CH_4 on the Sr pristine and Sr step surface is the weakest (0.10 eV); therefore, one could expect weaker adsorption of methane as the concentration of Sr at the surface increases. Subambient DRIFTS experiments were performed to corroborate computational insights about the interaction of CH_4 with different STO surfaces; namely, the enrichment of Sr at the surface weakens the adsorption of methane. After adsorption of CH_4 on the catalyst surface for 10 min at −146 °C, desorption of surface species was monitored via infrared spectroscopy (Figure 6). Adsorption of methane on surface-Ti-rich STO was stronger than on surface-Sr-rich STO, as the relative intensity of the vibrational modes around ∼2870 cm^{-1} (Figure 6a,b) and ∼2885 cm^{-1} (Figure 6c,d), attributed to the activated C−H bond in adsorbed methane,[45−47] decreased as the fraction of Sr at the surface increased. These experimental results corroborate predictions made by DFT regarding weaker CH_4 adsorption on Sr-richer STO surfaces (Table 2); and thus, they support the reliability of the computational results regarding energetic barriers for CH_4 activation. In fact, STO_{HT} samples (the set with the highest CH_4 conversion rates) showed negligible adsorption of CH_4 (Figure 6e−g). It is noteworthy that CH_4 presented stronger adsorption on surface-Ti-rich STO than on the single metal oxide TiO_2 (Figure S14). Enrichment of Ti at the surface of STO might be of interest for processes where strong CH_4 adsorption is desirable; however, such exploration lies beyond the scope of this work, and it must be kept in mind that DFT-based adsorption energies can only be related to experimental catalytic performances through careful microkinetic modeling.

CONCLUSIONS

In conclusion, the surface composition of $SrTiO_3$ (STO) was successfully tuned in a broad range via different synthetic

DOI: 10.1021/acscatal.8b02307
ACS Catal. 2018, 8, 10306−10315

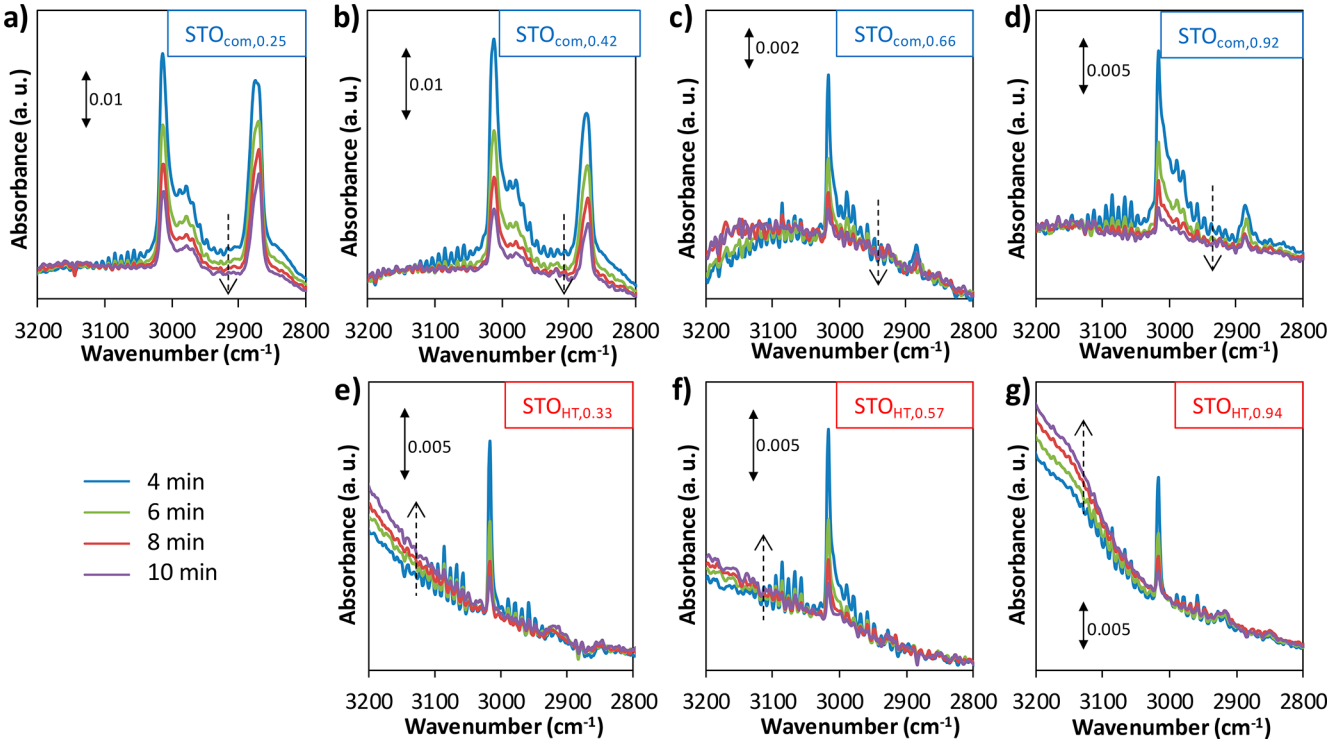

Figure 6. DRIFTS spectra of CH_4 desorption after 4, 6, 8, and 10 min at −146 (±4) °C, following adsorption for 10 min over (a−d) commercial STO catalysts treated with chemical etching or IWI ($STO_{com,x}$) and (e−g) STO catalysts synthesized via the HT method ($STO_{HT,x}$). x represents the fraction Sr/(Sr + Ti) at the surface of the catalyst. Dashed arrows show the direction of longer desorption.

conditions and postsynthetic chemical and thermal treatments. This work shows that the composition of the catalyst subsurface dictates the composition of the top surface. This presents a direct connection between the composition of subsurface layers of a perovskite catalyst and the performance of the catalyst for CH_4 activation, since the concentration of Sr at the surface is shown to be a descriptor for catalytic activity for a subset of STO catalysts, and the density of stepped sites is put forth as qualitative descriptor for the whole set of STO catalysts under study. More specifically, the concentration of Sr at the top layers is proportional to the rate of methane combustion when two sets of STO catalysts are analyzed independently. Measurement of kinetic isotopic effects (KIE) showed CH_4 activation as the rate-determining step (instead of O_2 activation) and showed that the energetic barrier for CH_4 activation on all samples studied is similar. This suggested that enhanced rates for STO_{HT} samples are due to more abundant active sites for CH_4 activation, not necessarily sites with different activation energies. Electron microscopy (HAADF-STEM) showed that the STO_{HT} samples have more abundant step sites at the surface, putting forward the hypothesis that step sites are more favorable for CH_4 activation. Indeed, DFT simulations showed that Sr step surfaces provide the lowest activation barrier for methane dissociation. Since the value of CD_4 KIE is approximately the same for all samples studied, we conclude that the step sites are present on all samples, but the abundance of these sites is what derives in different rates per surface area. Thus, the higher rates for STO_{HT} catalysts compared to STO_{com} catalysts are a consequence of higher density of active sites (Sr step site) as a result of surface and subsurface reconstruction. Subambient DRIFTS experiments provide further support to DFT predictions on the adsorption strength of CH_4 on STO surfaces, which reinforces the reliability of the DFT-predicted activation barriers.

With growing research efforts in methane catalysis, we have shown through atomic-level experimental and computational catalyst characterization, and kinetic isotopic experiments, that surface reconstruction of perovskites may be well capitalized for advanced catalyst design toward efficient methane activation.

■ ASSOCIATED CONTENT

Supporting Information

The Supporting Information is available free of charge on the ACS Publications website at DOI: 10.1021/acscatal.8b02307.

Additional text and equations, 14 figures, and four tables with description of catalysts under study, reactivity data, fitting to kinetic rate expression, tests for mass transfer limitation and effect of space velocity, XRD patterns, LEIS and XPS survey spectra, sample composition according to XPS, LEIS depth profiling, rates of methane conversion, calculation of theoretical KIE, HAADF-STEM images, and DRIFTS spectra of CH_4 desorption (PDF)

■ AUTHOR INFORMATION

Corresponding Author

*E-mail wuz1@ornl.gov.

ORCID

Zachary D. Hood: 0000-0002-5720-4392
Miaofang Chi: 0000-0003-0764-1567
De-en Jiang: 0000-0001-5167-0731
Zili Wu: 0000-0002-4468-3240

Present Addresses

▽(E.E.B.) Davidson School of Chemical Engineering, Purdue University, West Lafayette, IN 47907.

DOI: 10.1021/acscatal.8b02307
ACS Catal. 2018, 8, 10306−10315

◆(G.S.F.) W. L. Gore and Associates, Newark, DE 19711

Notes

The authors declare no competing financial interest.

■ ACKNOWLEDGMENTS

We thank Henry Luftman (Lehigh University) for performing LEIS analysis. This research was sponsored by the U.S. Department of Energy, Office of Science, Office of Basic Energy Sciences, Chemical Sciences, Geosciences, and Biosciences Division. Parts of the work including electron microscopy (X.L. and M.C.), DRIFTS, BET, and kinetic measurement were conducted at the Center for Nanophase Materials Sciences (CNMS), which is a DOE Office of Science User Facility. This research used resources of the National Energy Research Scientific Computing Center, a DOE Office of Science User Facility supported by the Office of Science of the U.S. Department of Energy under Contract DE-AC02-05CH11231. This manuscript has been authored by UT-Battelle, LLC, under Contract DE-AC05-00OR22725 with the U.S. Department of Energy. The United States Government retains and the publisher, by accepting the article for publication, acknowledges that the United States Government retains a nonexclusive, paid-up, irrevocable, worldwide license to publish or reproduce the published form of this manuscript, or allow others to do so, for United States Government purposes. The Department of Energy will provide public access to these results of federally sponsored research in accordance with the DOE Public Access Plan (http://energy.gov/downloads/doe-public-access-plan)

■ REFERENCES

(1) U.S. Energy Information Administration. *Annual Energy Outlook* 2018; https://www.eia.gov/outlooks/aeo/.

(2) Chen, J.; Arandiyan, H.; Gao, X.; Li, J. Recent Advances in Catalysts for Methane Combustion. *Catal. Surv. Asia* **2015**, *19*, 140−171.

(3) Gélin, P.; Primet, M. Complete oxidation of methane at low temperature over noble metal based catalysts: a review. *Appl. Catal., B* **2002**, *39*, 1−37.

(4) Choudhary, T. V.; Banerjee, S.; Choudhary, V. R. Catalysts for combustion of methane and lower alkanes. *Appl. Catal., A* **2002**, *234*, 1−23.

(5) Solomon, S., Qin, D., Manning, M., Chen, Z., Marquis, M., Averyt, K. B., Tignor, M., Miller, H. L., Eds.; *Climate Change 2007: The Physical Science Basis*; Contribution of Working Group I to the Fourth Assessment Report of the Intergovernmental Panel on Climate Change, 2007; Cambridge University Press: Cambridge, U.K.; http://www.ipcc.ch/publications_and_data/ar4/wg1/en/contents.html .

(6) Li, Z.; Hoflund, G. B. A Review on Complete Oxidation of Methane at Low Temperatures. *J. Nat. Gas Chem.* **2003**, *12*, 153−160 (http://www.academia.edu/10254796/A_Review_on_Complete_Oxidation_of_Methane_at_Low_Temperatures) .

(7) Royer, S.; Duprez, D.; Can, F.; Courtois, X.; Batiot-Dupeyrat, C.; Laassiri, S.; Alamdari, H. Perovskites as Substitutes of Noble Metals for Heterogeneous Catalysis: Dream or Reality. *Chem. Rev.* **2014**, *114*, 10292−10368.

(8) Ladavos, A.; Pomonis, P., Methane Combustion on Perovskites. In *Perovskites and Related Mixed Oxides*; Wiley−VCH: 2016; DOI: 10.1002/9783527686605.ch16.

(9) Zhu, J.; Li, H.; Zhong, L.; Xiao, P.; Xu, X.; Yang, X.; Zhao, Z.; Li, J. Perovskite Oxides: Preparation, Characterizations, and Applications in Heterogeneous Catalysis. *ACS Catal.* **2014**, *4*, 2917−2940.

(10) Martirez, J. M. P.; Kim, S.; Morales, E. H.; Diroll, B. T.; Cargnello, M.; Gordon, T. R.; Murray, C. B.; Bonnell, D. A.; Rappe, A. M. Synergistic Oxygen Evolving Activity of a TiO_2-Rich Reconstructed $SrTiO_3$(001) Surface. *J. Am. Chem. Soc.* **2015**, *137*, 2939−2947.

(11) Seitz, L. C.; Dickens, C. F.; Nishio, K.; Hikita, Y.; Montoya, J.; Doyle, A.; Kirk, C.; Vojvodic, A.; Hwang, H. Y.; Norskov, J. K.; Jaramillo, T. F. A highly active and stable $IrO_x/SrIrO_3$ catalyst for the oxygen evolution reaction. *Science* **2016**, *353*, 1011−1014.

(12) Fabbri, E.; Nachtegaal, M.; Binninger, T.; Cheng, X.; Kim, B.-J.; Durst, J.; Bozza, F.; Graule, T.; Schäublin, R.; Wiles, L.; Pertoso, M.; Danilovic, N.; Ayers, K. E.; Schmidt, T. J. Dynamic surface self-reconstruction is the key of highly active perovskite nano-electrocatalysts for water splitting. *Nat. Mater.* **2017**, *16*, 925−932.

(13) Koocher, N. Z.; Martirez, J. M. P.; Rappe, A. M. Theoretical Model of Oxidative Adsorption of Water on a Highly Reduced Reconstructed Oxide Surface. *J. Phys. Chem. Lett.* **2014**, *5*, 3408−3414.

(14) Peng, Y.; Si, W.; Luo, J.; Su, W.; Chang, H.; Li, J.; Hao, J.; Crittenden, J. Surface Tuning of $La_{0.5}Sr_{0.5}CoO_3$ Perovskite Catalysts by Acetic Acid for NO_x Storage and Reduction. *Environ. Sci. Technol.* **2016**, *50*, 6442−6448.

(15) Wang, X.; Huang, K.; Qian, J.; Cong, Y.; Ge, C.; Feng, S. Enhanced CO catalytic oxidation by Sr reconstruction on the surface of $La_xSr_{1-x}CoO_{3-\delta}$. *Sci. Bull.* **2017**, *62*, 658−664.

(16) Polo-Garzon, F.; Yang, S. Z.; Fung, V.; Foo, G. S.; Bickel, E. E.; Chisholm, M. F.; Jiang, D. e.; Wu, Z. Controlling Reaction Selectivity through the Surface Termination of Perovskite Catalysts. *Angew. Chem.* **2017**, *129*, 9952−9956.

(17) Foo, G. S.; Hood, Z. D.; Wu, Z. Shape Effect Undermined by Surface Reconstruction: Ethanol Dehydrogenation over Shape-Controlled $SrTiO_3$ Nanocrystals. *ACS Catal.* **2018**, *8*, 555−565.

(18) Ngai, J. H.; Schwendemann, T. C.; Walker, A. E.; Segal, Y.; Walker, F. J.; Altman, E. I.; Ahn, C. H. Achieving A-Site Termination on $La_{0.18}Sr_{0.82}Al_{0.59}Ta_{0.41}O_3$ Substrates. *Adv. Mater.* **2010**, *22*, 2945−2948.

(19) Druce, J.; Tellez, H.; Burriel, M.; Sharp, M. D.; Fawcett, L. J.; Cook, S. N.; McPhail, D. S.; Ishihara, T.; Brongersma, H. H.; Kilner, J. A. Surface termination and subsurface restructuring of perovskite-based solid oxide electrode materials. *Energy Environ. Sci.* **2014**, *7*, 3593−3599.

(20) Fu, Q.; Wagner, T. Interaction of nanostructured metal overlayers with oxide surfaces. *Surf. Sci. Rep.* **2007**, *62*, 431−498.

(21) Martirez, J. M. P. Surface Reconstructions of Perovskite-Type Oxides: Their Exotic Structures and Modified Chemistry. Ph.D. Dissertation, University of Pennsylvania, 2015; https://repository.upenn.edu/edissertations/1094 (accessed May 20, 2018).

(22) Dagdeviren, O. E.; Simon, G. H.; Zou, K.; Walker, F. J.; Ahn, C.; Altman, E. I.; Schwarz, U. D. Surface phase, morphology, and charge distribution transitions on vacuum and ambient annealed $SrTiO_3$(100). *Phys. Rev. B: Condens. Matter Mater. Phys.* **2016**, *93*, No. 195303.

(23) Nishimura, T.; Ikeda, A.; Namba, H.; Morishita, T.; Kido, Y. Structure change of TiO_2-terminated $SrTiO_3$(001) surfaces by annealing in O_2 atmosphere and ultrahigh vacuum. *Surf. Sci.* **1999**, *421*, 273−278.

(24) Jiang, Q. D.; Zegenhagen, J. c(6 × 2) and c(4 × 2) reconstruction of $SrTiO_3$(001). *Surf. Sci.* **1999**, *425*, 343−354.

(25) Erdman, N.; Warschkow, O.; Asta, M.; Poeppelmeier, K. R.; Ellis, D. E.; Marks, L. D. Surface Structures of $SrTiO_3$ (001): A TiO_2-rich Reconstruction with a c(4 × 2) Unit Cell. *J. Am. Chem. Soc.* **2003**, *125*, 10050−10056.

(26) Erdman, N.; Poeppelmeier, K. R.; Asta, M.; Warschkow, O.; Ellis, D. E.; Marks, L. D. The structure and chemistry of the TiO_2-rich surface of $SrTiO_3$ (001). *Nature* **2002**, *419*, 55−58.

(27) Heifets, E.; Piskunov, S.; Kotomin, E. A.; Zhukovskii, Y. F.; Ellis, D. E. Electronic structure and thermodynamic stability of double-layered $SrTiO_3$(001) surfaces: *Ab initio* simulations. *Phys. Rev. B: Condens. Matter Mater. Phys.* **2007**, *75*, No. 115417.

(28) Wang, Z.; Loon, A.; Subramanian, A.; Gerhold, S.; McDermott, E.; Enterkin, J. A.; Hieckel, M.; Russell, B. C.; Green, R. J.; Moewes, A.; Guo, J.; Blaha, P.; Castell, M. R.; Diebold, U.; Marks, L. D.

DOI: 10.1021/acscatal.8b02307
ACS Catal. 2018, 8, 10306−10315

Transition from Reconstruction toward Thin Film on the (110) Surface of Strontium Titanate. *Nano Lett.* **2016**, *16*, 2407−2412.
(29) Lin, Y.; Wen, J.; Hu, L.; Kennedy, R. M.; Stair, P. C.; Poeppelmeier, K. R.; Marks, L. D. Synthesis-Dependent Atomic Surface Structures of Oxide Nanoparticles. *Phys. Rev. Lett.* **2013**, *111*, No. 156101.
(30) Kwapien, K.; Paier, J.; Sauer, J.; Geske, M.; Zavyalova, U.; Horn, R.; Schwach, P.; Trunschke, A.; Schlögl, R. Sites for Methane Activation on Lithium-Doped Magnesium Oxide Surfaces. *Angew. Chem., Int. Ed.* **2014**, *53*, 8774−8778.
(31) Choudhary, V. R.; Mulla, S. A. R.; Uphade, B. S. Oxidative Coupling of Methane over SrO Deposited on Different Commercial Supports Precoated with La_2O_3. *Ind. Eng. Chem. Res.* **1998**, *37*, 2142−2147.
(32) Chen, Y.-W.; Chen, H.-Y.; Lin, W.-F. Basicities of alumina-supported alkaline earth metal oxides. *React. Kinet. Catal. Lett.* **1998**, *65*, 83−86.
(33) Dong, L.; Shi, H.; Cheng, K.; Wang, Q.; Weng, W.; Han, W. Shape-controlled growth of $SrTiO_3$ polyhedral submicro/nanocrystals. *Nano Res.* **2014**, *7*, 1311−1318.
(34) Mu, L.; Zhao, Y.; Li, A.; Wang, S.; Wang, Z.; Yang, J.; Wang, Y.; Liu, T.; Chen, R.; Zhu, J.; Fan, F.; Li, R.; Li, C. Enhancing charge separation on high symmetry $SrTiO_3$ exposed with anisotropic facets for photocatalytic water splitting. *Energy Environ. Sci.* **2016**, *9*, 2463−2469.
(35) Dong, L.; Luo, Q.; Cheng, K.; Shi, H.; Wang, Q.; Weng, W.; Han, W.-Q. Facet-Specific Assembly of Proteins on $SrTiO_3$ Polyhedral Nanocrystals. *Sci. Rep.* **2015**, *4*, No. 5084.
(36) Brunauer, S.; Emmett, P. H.; Teller, E. Adsorption of Gases in Multimolecular Layers. *J. Am. Chem. Soc.* **1938**, *60*, 309−319.
(37) Kresse, G.; Furthmüller, J. Efficiency of ab-initio total energy calculations for metals and semiconductors using a plane-wave basis set. *Comput. Mater. Sci.* **1996**, *6*, 15−50.
(38) Kresse, G.; Furthmüller, J. Efficient iterative schemes for ab initio total-energy calculations using a plane-wave basis set. *Phys. Rev. B: Condens. Matter Mater. Phys.* **1996**, *54*, 11169−11186.
(39) Perdew, J. P.; Burke, K.; Ernzerhof, M. Generalized Gradient Approximation Made Simple. *Phys. Rev. Lett.* **1996**, *77*, 3865−3868.
(40) Kresse, G.; Joubert, D. From ultrasoft pseudopotentials to the projector augmented-wave method. *Phys. Rev. B: Condens. Matter Mater. Phys.* **1999**, *59*, 1758−1775.
(41) Blöchl, P. E. Projector augmented-wave method. *Phys. Rev. B: Condens. Matter Mater. Phys.* **1994**, *50*, 17953−17979.
(42) Monkhorst, H. J.; Pack, J. D. Special points for Brillouin-zone integrations. *Phys. Rev. B* **1976**, *13*, 5188−5192.
(43) Henkelman, G.; Uberuaga, B. P.; Jónsson, H. A climbing image nudged elastic band method for finding saddle points and minimum energy paths. *J. Chem. Phys.* **2000**, *113*, 9901−9904.
(44) Schwach, P.; Pan, X.; Bao, X. Direct Conversion of Methane to Value-Added Chemicals over Heterogeneous Catalysts: Challenges and Prospects. *Chem. Rev.* **2017**, *117*, 8497−8520.
(45) Li, C.; Li, G.; Xin, Q. FT-IR Spectroscopic Studies of Methane Adsorption on Magnesium Oxide. *J. Phys. Chem.* **1994**, *98*, 1933−1938.
(46) Li, C.; Yan, W.; Xin, Q. Interaction of methane with surface of alumina studied by FT-IR spectroscopy. *Catal. Lett.* **1994**, *24*, 249−256.
(47) Thomasson, P.; Tyagi, O. S.; Knözinger, H. Characterisation of the basicity of modified MgO-catalysts. *Appl. Catal., A* **1999**, *181*, 181−188.

DOI: 10.1021/acscatal.8b02307
ACS Catal. 2018, 8, 10306−10315